



# Design, manufacturing and validation of a vertical-axis wind turbine setup for wind tunnel tests

A. Vergaerde<sup>a</sup>, T. De Troyer<sup>a,\*</sup>, A. Carbó Molina<sup>a,b</sup>, L. Standaert<sup>a</sup>, M.C. Runacres<sup>a</sup>

<sup>a</sup> Vrije Universiteit Brussel, Pleinlaan 2, 1050, Brussels, Belgium

<sup>b</sup> Università degli Studi di Firenze, Via di Santa Marta 3, 50139, Firenze, Italy

## ARTICLE INFO

### Keywords:

VAWTs  
Design process  
Structural analysis  
Modal analysis  
Spectral analysis  
Wind tunnel tests

## ABSTRACT

The potential of vertical-axis wind turbines (VAWTs) for specific applications (floating off-shore or urban installations) has been reconsidered in recent years. This renewed interest has led to an increasing number of experimental studies on VAWTs. A challenge of experimental work is correctly interpreting experimental results but just as important is the design of the experimental setup. The objective of the present study is to elaborate on the complete development process of a VAWT wind tunnel test setup, from design to aerodynamic interpretation. The effect of the design choices and structural characteristics of the setup can be traced in the measured torque. The influence of structural dynamics of an experimental setup are proven to influence unsteady measurements significantly through the analysis of the spectral content of the measured torque. An extensive modal analysis of the VAWT rotor allows to link modal vibrations to their contaminating effect on the measured torque. In addition, the dynamics of the sensors and setup are found to be important contributions to the contamination of dynamic measurements. To interpret unsteady torque measurements, the complete experimental setup needs to be dynamically characterised.

## 1. Introduction

The Darrieus vertical-axis wind turbine (VAWT) was extensively studied in the 1970s and 80s (see, e.g., (Sheldahl et al., 1980; Paraschivoiu, 1981; Akins et al., 1987)), but then further development stalled as the focus was almost exclusively on the horizontal-axis wind turbine (HAWT) concept (Sutherland et al., 2012). nicely summarises the state of the art in VAWT technology up to the early 1990s, while (Paraschivoiu, 2002) describes the numerical models that were then available for design and simulation of VAWTs.

Since about 2010, a renewed interest has been given to Darrieus VAWTs, mainly because of the presumed advantages for deep off-shore, floating installations (Paulsen et al., 2013; Shires, 2013; Borg et al., 2014). Several research and development projects have been undertaken in academia as well as the industry (e.g. Spinfloat by EOLFI, Twinfloat by Nenuphar, or the EU-funded project DeepWind). In this wake, also more fundamental research (e.g. on VAWT blade aerodynamics as by (Simão Ferreira and Geurts, 2015)) or on improved numerical models (see e.g. (Chatelain et al., 2007) or (Simão Ferreira et al., 2014)) has emerged.

Besides off-shore installations, VAWTs have also been suggested for use in urban environments (Balduzzi et al., 2012; Bertényi et al., 2010;

Molina et al., 2018; van Bussel and Mertens). VAWTs are expected to respond better to the complex and highly-turbulent flow of urban environments when compared with HAWTs (Möllerström et al., 2016; Bertényi et al., 2010).

Despite these potential advantages, Darrieus VAWTs are intrinsically limited to lower efficiencies than HAWTs, because of the continuously varying angle of attack ( $\alpha$ ) and because the blades move in their own wake part of each rotation. A lot of the ongoing research is oriented towards mitigating these inherent limitations (Huijs et al., 2018; Bayati et al., 2018; Greenblatt et al., 2012; Dabiri, 2011; Duraisamy and Lakshminarayan, 2014; Zanforlin and Nishino, 2016; Vergaerde et al., 2018).

Many of these studies were done using numerical simulations, and though this offers obvious benefits, the experimental validation under controlled circumstances in the wind tunnel is warranted.

Undeniably, experimental wind tunnel studies do suffer from the difficulty of reproducing the physics of full-scale models in a lab environment. Studies such as (Bachant and Wosnik, 2016) and (Miller et al., 2018) indicate that the performance of a VAWT is indeed influenced by a Reynolds number effect. Furthermore, the aerodynamic and structural performance of an experimental VAWT is also strongly influenced by

\* Corresponding author.

E-mail address: [tim.de.troyer@vub.be](mailto:tim.de.troyer@vub.be) (T. De Troyer).

<https://doi.org/10.1016/j.jweia.2019.103949>

Received 26 March 2019; Received in revised form 21 May 2019; Accepted 4 July 2019

Available online 1 August 2019

0167-6105/© 2019 Elsevier Ltd. All rights reserved.

(modal) vibrations. In 1991, Sandia researchers (Clark, 1991) programmed the controller of their 50m-high  $\varphi$ -type VAWT based on a modal analysis to exclude certain rpms. On a smaller scale, such modal vibrations influence aerodynamic measurements (McLaren et al., 2012). were forced to develop a vibration isolation methodology to allow better aerodynamic measurements of their high-solidity VAWT (Mabrouk et al., 2017). studied the impact of the unsteady VAWT-aerodynamics on the drive train while (Asr et al., 2017) have approached the modal analysis of VAWTs through finite element analyses allowing to characterise the effect of radial forces (related to the rotational speed) on modal vibrations.

To capture the performance of an experimental VAWT model, it is possible to directly measure aerodynamic forces (Peng et al., 2019), or to measure the local pressure on a VAWT aerofoil (Li et al., 2016). Such measurements require structural modifications of the rotor itself (hence also altering the dynamic behaviour of the rotor).

In the present study, a direct-drive torque sensor is used to quantify the performance of a VAWT model. Similar setups have been used previously to study the potential of a variable-pitch system (Elkhoury et al., 2015) or to study the effect of the number of blades (Li et al., 2015).

In the present study, the effect of design choices and manufacturing methodology are traced in the aerodynamic performance of the VAWT rotor. The interpretation of the unsteady aerodynamics of an experimental VAWT is complicated because of contamination of the torque measurements. Through an extensive characterisation of the setup, torque losses, sensor dynamics, external inputs, natural frequencies and modal vibrations of the rotor are found to be the major responsible factors for this contamination. Signal processing allows to identify these contaminations.

Therefore, the objective of this article is to detail the design, manufacturing, and validation of a VAWT wind tunnel scale model, developed at the Vrije Universiteit Brussel. Mechanical, structural, and aerodynamic characteristics of the model and its components are presented to serve as a benchmark for future VAWT wind tunnel tests. In doing so, this article complements recent reports on VAWT experiments that focussed on blockage corrections (Dossena et al., 2015), set-ups with individual pitch control (LeBlanc and Simao Ferreira, 2018; Bayati et al., 2018), aeroelastic effects and torque control (Bottasso et al., 2014), or Reynolds number effects (Miller et al., 2018).

The structure of the article is as follows. First, the design requirements of the rotor are introduced. Then the manufacturing of the rotor is discussed, followed by a structural analysis of the rotor and a complete mechanical and aerodynamic characterization of the set-up.

## 2. Design parameters of the rotor

VAWTs appear to have several perceived advantages with promising characteristics regarding their power production. Two of such advantages are:

1. VAWTs produce more power when placed in paired configurations (Vergaerde et al., 2018; Dabiri, 2011);
2. A turbulent environment, such as an urban environment, exhibits beneficial characteristics for the power production of VAWTs (Molina et al., 2018).

To analyse the two above-mentioned advantages, rotor models of VAWTs were designed, manufactured and characterised for wind tunnel tests.

One objective of this experimental work is to validate numerical simulations (previously in collaboration with the French company Nenuphar). Preliminary numerical modelling through CFD and a vortex-methods-based code (ARDEMA, (Parneix et al., 2016),) was carried out by Nenuphar. These models allowed to conclude that in order to have similar aerodynamics as for a larger scale VAWT rotor, the minimal required chord-Reynolds number,  $Re_c$ , is  $1 \times 10^5$ . Conditions below this Reynolds number involved too small aerodynamic forces as to allow

experimentally relevant conclusions. This led to the condition to operate the models at chord-based Reynolds numbers above  $1 \times 10^5$ , given by the following equation:

$$\overline{Re}_c = \frac{c\lambda U_0}{\nu} \quad (1)$$

It is an average Reynolds number as the chord-based Reynolds number varies throughout one complete rotation where  $c$  is the blade-chord,  $U_0$  the unperturbed windspeed,  $\lambda$  the tip-speed ratio and the kinematic viscosity of air,  $\nu$ . On the other hand, structural limitations forced the suppression of rotational speeds, inducing substantial centrifugal forces. The lower limit for the operational chord-based Reynolds number was thus set to  $1 \times 10^5$ .

The designed models are H-type Darrieus VAWTs with inclined struts (see Fig. 1). H-type VAWTs have been used before to demonstrate their potential as pairs in open field tests (Dabiri, 2011). This H-type design (as well as the Y-type design) enables the possibility for a shorter rotor tower compared to equivalent VAWTs of another type. A shorter tower reduces the aerodynamic losses as a result of the reduced span of the tower wake (inevitably, downwind passing blades pass through the wake of the tower). As mentioned, the struts are inclined which is beneficial as they contribute to the total torque generation of the rotor while also allowing to reduce the size of the central hub.

In terms of blade numbers, both the two-bladed and three-bladed configuration present advantages and disadvantages compared to each other (Sutherland et al., 2012). Here, the two-bladed design was favoured as this design is easier to balance from both a structural and aerodynamic point of view. The fact, however, of having symmetrical aerodynamic forces, induces a larger torque ripple and poorer structural dynamics compared to a three-bladed design. This is one of the many conclusions of studies focussing on the effect of solidity and number of blades, through an experimental approach (Li et al., 2015) or simulations (Delafin et al., 2016; Rezaeiha et al., 2018; Cheng et al., 2017). With a third or forth blade and an increase of the solidity the optimal power coefficient of the turbine could be improved. This would, however, be mostly beneficial for lower wind speeds. For large-scale VAWTs, the two-bladed design is easier to mount since it allows ground-level assembly. To the present case, this assembly advantage corresponds to the fact that the rotors are easier to transport.

The two blades (NACA0018,  $c = 50$  mm), are connected to the central hub with two struts (NACA0024,  $c = 30$  mm) per blade. The blades of a VAWT are exposed to dynamic conditions with constantly changing angles of attack. A NACA0018 blade was chosen as its thickness provides a good resistance against bending stress and exhibits favourable aerodynamic characteristics (maximum lift coefficient around 1.1, relatively

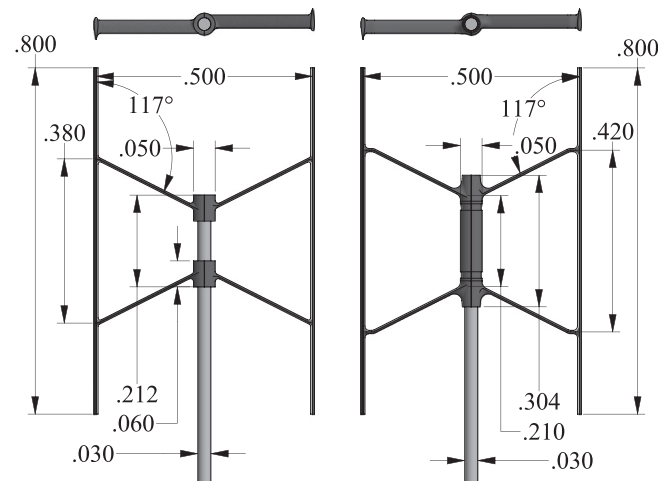


Fig. 1. VAWT rotor Gen1, right: VAWT rotor Gen2. Units are in m.

mild stall behaviour around  $11^\circ$ ). The thicker NACA0024 struts were favoured predominantly because of their thickness providing extra structural strength. The smaller chord length of the struts allows to keep a clean leading edge and trailing edge over the full span of the blades (see top of Fig. 1).

Design wise, the operational chord-based Reynolds number sets a lower limit for the chord-unperturbed speed product ( $cU_0$ ), as  $\lambda$  will be in the range 2–4 (based on numerical simulations (Parneix et al., 2016)). This  $cU_0$  -product influences the optimal rotor solidity,  $\sigma$ , and the design tip-speed ratio, based on the ratio of the rotational speed,  $\Omega$ , and  $U_0$ , which are defined as:

$$\sigma = \frac{cb}{D}, \quad (2)$$

$$\lambda = \frac{\Omega(D/2)}{U_0}. \quad (3)$$

The solidity of the rotors (with diameter,  $D$  and number of blades,  $b$ ) is 0.20. Increasing the solidity allows for a slightly higher maximum power coefficient but it reduces the operating range significantly (Paraschivoiu, 2002).

It is the combination of the solidity, the number of blades and the aspect ratio that defines most of the geometric parameters for the VAWT rotor design. Here, the aspect ratio (defined by the ratio of height,  $H$ , to  $D$ ) of the rotors is 1.6 ( $H = 0.800\text{m}$ ,  $D = 0.500\text{m}$ ). Paraschivoiu states that an aspect ratio between 1.3 and 1.5 is optimal (Paraschivoiu, 2002). For lower Reynolds numbers, a higher aspect ratio seems to be advantageous for the VAWT performance (Brusca et al., 2014). Moreover, for further testing a higher aspect ratio will induce a larger interaction between two closely-spaced VAWTs for a given frontal surface.

The small radius of the rotors induces a relatively high rotational speed (ranging between 900 and 1350 rpm). Here the relatively high solidity is beneficial as a high-solidity turbine reaches its optimal performance at lower tip-speed ratios (directly influencing the optimal rotational speed at a given wind speed).

Two iterations of the rotor designs were designed and manufactured for wind tunnel tests, referred to as Generation 1 (Gen1) (Fig. 1, left) and Generation 2 (Gen2) (Fig. 1, right). All the aforementioned design parameters are valid for both generations. Their design, however, exhibits some differences. The original design, Gen1 rotor, suffered from torsional weakness. The two-part hub did not provide sufficient torsional stiffness which caused the vertical blades to tilt during operation giving them an uncontrolled twist angle comparable to a helical-type VAWT. The Gen2 rotor is stiffer due to its larger one-part hub. The influence of this larger hub seems to slightly degrade the performance of the models and is traceable in near-wake measurements (see Section 5.3 and 5.7). Another difference between the two generations is their strut ratio (SR) which is defined as the ratio between the total length of the blade and the length of the blade section between the struts. The SR was calculated so as to allow identical deflection between the tip ends and the blade centre. However, image analysis of the Gen1 rotors in operation showed that it allowed a larger tip deflection compared to the blade-centre. To reduce the tip deflection and allow a larger blade-centre deflection, the original SR of 2.12 was reduced to 1.90 for the Gen2 design. The updated SR minimises the deflection of the blade tips and is thus beneficial for the reduction of the stress inside the structure of the rotor (see Section 4.3).

Table 1 summarizes the rotor design and its operational parameters.

### 3. Manufacturing methodology of the models

#### 3.1. Manufacturing methodology

One of the most important structural requirements was imposed by the centrifugal forces acting on the rotor during operation. The operating rotational speed was calculated to range around 1100 rpm and for a

**Table 1**

Geometric design and operational parameters of the rotors.

	Gen1/Gen2 rotor
Rotor type	H-Darrieus
Number of blades	2
Diameter, $D$ [m]	0.500
Height, $H$ [m]	0.800
Blade chord, $c$ [m]	0.050
Strut chord [m]	0.030
Strut angle [°]	117
Blade aerofoil	NACA0018
Strut aerofoil	NACA0024
Strut ratio, SR	Gen1: 2.12 Gen2: 1.90
Solidity, $\sigma$	0.2
Tip-speed ratio, $\lambda$	2.4–3.4
Optimal tip-speed ratio, $\lambda(C_{P,max})$	3.0
Operational rotational speed, $\Omega$ [rpm]	900–1350

safety factor of 1.4 the rotor had to withstand rotational speeds of 1800 rpm. This forced the adoption of strong, lightweight carbon-fibre composites for the production of the rotors. Between the considered and tested composite manufacturing processes (vacuum bag moulding, vacuum infusion processing, compression moulding with pressurised bag and compression moulding with mould-counter-mould), it was the mould-counter-mould technique that presented the best geometrical results.

The moulds were originally CNC-milled out of a high-density polyurethane (HDPU) foam block with an accuracy of 0.02 mm. The demoulding process, however, appeared to damage the moulds substantially which is why the HDPU moulds were replaced with aluminium moulds (bringing along a substantial increase of the production cost). The effects of the damaged HDPU moulds are traceable in the performance of the Gen1 rotors and are readdressed in Section 5.3.

#### 3.2. Aerodynamic validation of the manufacturing methodology

In order to validate the selected manufacturing methodology aerodynamically, two manufactured aerofoils (NACA0018) were tested in the wind tunnel. The aerofoils have a chord of 0.050m and a span of 0.800m which correspond to the dimensions of the blades on the VAWT rotors. The low-speed wind tunnel of the VUB allows maximum speeds of 20 m/s which corresponds to a maximum Reynolds number of  $6 \times 10^4$  at which these tests occurred. For these wind tunnel tests, no leading edge tripping is done to fix the transition of the boundary layer because of the small dimensions. The aerofoils were mounted on a six-component aerodynamic balance and end plates were fixed at the extremities of the blades to avoid tip-losses. The recorded forces were decomposed in the aerodynamic lift and drag and compared with the literature as seen for the lift coefficient in Fig. 2. In this figure, the blue dots represent the experimental results of the first blade while the orange crosses represent the experimental results of the second one. The dashed line corresponds to an interpolation of the data of Sheldahl and Klimas (1981) between Reynolds number  $4 \times 10^4$  and  $8 \times 10^4$  while the dotted line corresponds to the data acquired by Timmer (Timmer, 2008) but at a higher Reynolds number of  $15 \times 10^4$ .

These results indicate similar aerodynamic properties: their optimal lift coefficients,  $C_L$ , exhibit similar magnitudes, both aerofoils stall around similar  $\alpha$  and the slope of their  $C_L(\alpha)$  -curves is comparable. The similarity between positive and negative  $\alpha$  indicates the symmetry of the aerofoil.

### 4. Structural analysis of the rotor

Prior to wind tunnel testing, static and dynamic tests were performed to assess the structural integrity of the rotors. The Gen1 design was improved based on these static and dynamic tests. The structural analysis comprises a dynamic crash test, a static uniformly distributed load

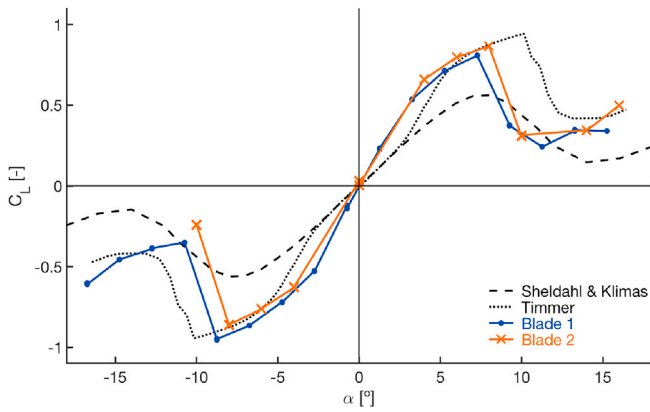


Fig. 2.  $C_L(\alpha)$  comparison of two manufactured NACA0018 blades (blue dots and orange crosses) at Reynolds  $6 \times 10^4$  with the Sheldahl and Klimas data (dashed line) and comparison to the data of Timmer (dotted line).

analysis and a static deflection test. This structural analysis is described in the following section.

#### 4.1. Ultimate load tests

Before entering the wind tunnel, the structural limits of the rotors were analysed with a dynamic crash test and/or a uniformly distributed static load analysis. The objective of these tests was to capture the critical rotational speeds of each design. The dedicated setup for each of these critical failure tests is similar: a horizontally mounted steel shaft between bearings inside a stiff aluminium frame (Fig. 3). For the dynamic crash tests specifically, the setup is equipped with a DC-motor to drive the rotors until failure.

##### 4.1.1. Preliminary prototype shortcomings

A Gen1 prototype was subjected to a dynamic crash test and appeared to suffer from delamination. The destructive dynamic test was terminated at 980 rpm, when the rotor blade separated from the strut. The centrifugal forces,  $F_{cf}$ , acting on the blade-strut connection at the moment of rupture corresponds to 632N according to:

$$F_{cf} = m_{blade} \Omega^2 (D/2), \quad (4)$$

with  $m_{blade}$  being the mass of the blade. Post video analysis of this test indicated that the fibre-layup methodology caused the epoxy to be stressed at the blade-strut connection. The layup technique was reviewed

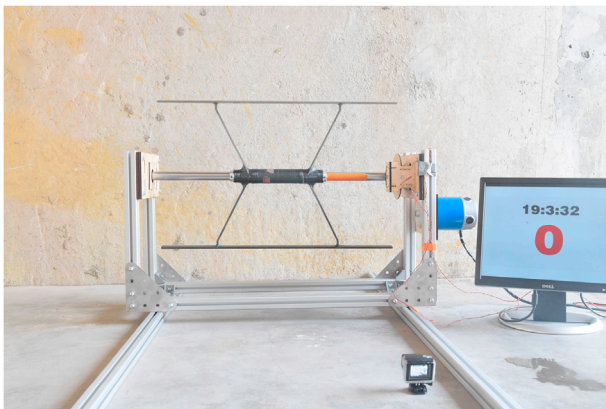


Fig. 3. Setup used for dynamic crash tests or, provided with minor modifications, for uniformly distributed static load analyses. Here a Gen2 rotor is mounted for a dynamic crash test.

in order to solely stress the carbon fibres. A schematic cross-section in Fig. 4 illustrates this reviewed layup technique with fibres going from the hub, through the strut, to the blade. These fibres were inserted as such that they run from the struts to the extremities of the blade, thereby crossing the fibres that run along the blade. This reviewed layup technique focusses on solely stressing the carbon fibres during operation.

##### 4.1.2. Uniformly distributed static load analysis

With a similar objective as the dynamic crash test, the uniformly distributed static load analysis focusses more specifically on the identification of delamination. It is possible to carry out this static test on a half rotor, saving both time and cost. Half of one Gen1 rotor was manufactured for this destructive structural test with the reviewed layup technique. This half rotor was mounted horizontally on the static testbench and an increasing load was applied on the blade. Critical failure was reached at a load of 1695 N, when the blade-strut connection fractured. In terms of centrifugal loads, this corresponds to a rotational speed of 1850 rpm (Equation (4)). The fracture indicated little delamination due to its brittle nature meaning that the structural limits of the fibres were reached. Another type of failure would suggest a flaw in the layup technique.

##### 4.1.3. Dynamic crash tests

Two Gen1 rotors were manufactured with the reviewed layup technique. On the dynamic testbench these rotors withstood rotational speeds around 1600 rpm. This rotational speed was considered to give a sufficiently safe margin as the Gen1 rotors operate between 900 and 1350 rpm. The test was ended without critical failure of a rotor in order to preserve them.

Contrary to the Gen1 rotors, the Gen2 rotors have been tested dynamically up to the point of critical failure. For the critical rotational speed (more than 2100 rpm), this failure corresponded to a centrifugal force of 2190 N per blade. Considering the operational range of the rotors during wind tunnel tests, this means that the rotor rotates at around 60% of its critical rotational speed.

Critical failure occurred again with a brittle fracture validating the carbon fibre configuration once more. To further increase the safety during operation, these Gen2 rotors are equipped with a Kevlar core to avoid the scattering of pieces in case of a failure.

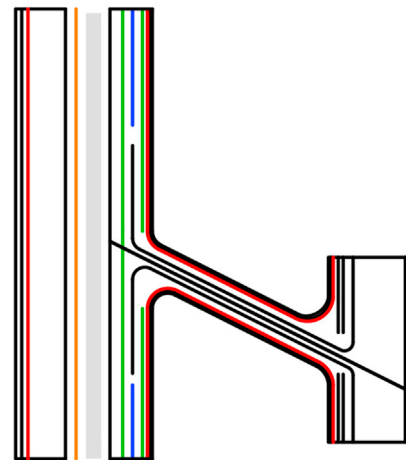


Fig. 4. Schematic representation of the carbon fibre configuration inside the rotor going from the hub (right), through the strut, to the blade (left) (not to scale). The thickness of the fibre weaves is 0.1 mm. The Gen2 also contains Kevlar fibres to avoid the scattering of pieces in case of failure. After the curing process, the edge thickness of the blade is 1.2 mm.



## 4.2. Static deformation tests

The elastic properties of the rotors were investigated statically by applying various loads on a rotor blade fixed as a cantilever. The deflections,  $\delta$ , were recorded and the Young's modulus,  $E$ , was estimated to be 38.5 GPa according to the following formula:

$$E = \frac{mgz^2(3l - z)}{I\delta}, \quad (5)$$

where  $l$  is the free length of the cantilever and  $g$ , the gravitational constant. The position where the applied loads with mass,  $m$ , act is represented with  $z$ . In Equation (5), the area moment of inertia,

$$I = \iint y^2 dA, \quad (6)$$

was considered with  $y$  being the perpendicular distance to the neutral line, i.e. the chord line. The surface of the hollow NACA0018 blades (with an edge thickness of 1.2 mm) is calculated based on the area of a NACA aerofoil.

Typically, the elastic properties of industrial carbon-fibre reinforced polymer (CFRP) result in a Young's modulus which ranges between 69 and 150 GPa. The value of this property is dependent of the carbon-epoxy ratio. The rotors were built with a 40% ratio which is lower than commonly achieved which explains the lower E-modulus.

## 4.3. Rotor stress and deflection analysis

To numerically estimate the bending stress and deflection of the rotor during operation it was reduced to a simpler model. The extremities of the blades were considered as a cantilever beam on which a uniformly distributed load,  $w$ , is applied. The part of the blade in-between the blade-strut connections, was considered as a clamped beam.

Structural analyses with CAD-software indicate that the highest stress inside the structure of the rotor occurs at the blade-strut connection. This was confirmed with image and video analysis of the dynamic crash test. The bending stress,  $\sigma_b$ , during operation in the blade-strut connection, is calculated using the flexure formula:

$$\sigma_b = \frac{wl^2t/2}{2I} \quad (7)$$

In this equation,  $l$  is the span of the blade length above and below the blade-strut connection point. Based on Equation (7), Fig. 5 represents the stress at the blade-strut connection of the Gen1 rotors with blue circles

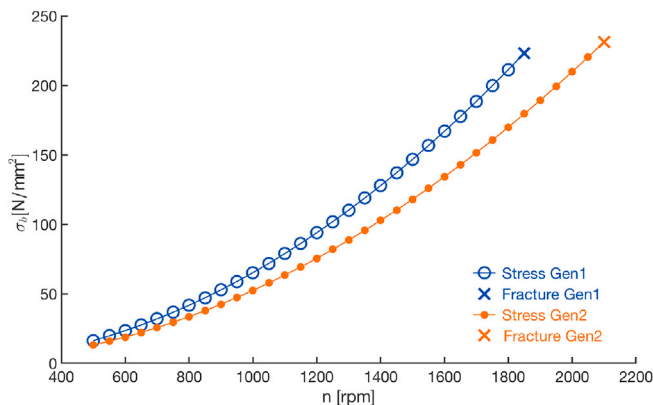


Fig. 5. Comparison of the stress at the blade-strut connection for increasing rotational speeds for the Gen1 design (blue circles) and the Gen2 design (orange dots). Their point of fracture is indicated with a cross. (For interpretation of the references to colour in this figure legend, the reader is referred to the Web version of this article.)

while the stress at the Gen2 blade-strut connection is indicated with orange dots. Here, the critical rotational speeds (experimentally determined from the previously described tests) are represented with crosses at the end of the curves.

With the results of the static deformation test and Equation (8), the deflection at the tips during operation is estimated. Similarly, using Equation (9), it is possible to estimate the deflection at the blade-centre:

$$\delta_{\max, \text{tip}} = \frac{wl^4}{8EI}, \quad (8)$$

$$\delta_{\max, \text{centre}} = \frac{5wl^4}{384EI}. \quad (9)$$

Solving Equations (8) and (9) results in a maximal deflection of 13.0 mm during operational conditions. Operational tests indicated a larger deflection of the rotor tips compared to the blade centre. In order to keep the deflection (and stress) minimal on both sides of the blade-strut connections, the Gen1 strut ratio of 2.12 was reduced to a strut ratio of 1.90 to equalise the deflection between the blade tips and the blade centre. This more optimal stress distribution allows to reach higher rotational speeds with the Gen2 design.

## 4.4. Experimental modal analysis

Inherently, a two-bladed VAWT induces symmetric loadings on the rotor which are important drivers for the in-plane and out-of-plane vibrational modes of the rotor (Sutherland et al., 2012). The vibrational modes of a Gen2 rotor were characterised by an experimental modal analysis. An impact hammer (Endevco model 2302 modal hammer) served as a trigger for three accelerometers (PCB model 333B32) which were placed respectively on both the blade upper tips and the hub upper tip. These unidirectional accelerometers measured the three perpendicular directions (XYZ). The used data-acquisition software was Siemens LMS Simcenter Test Lab. Two different configurations were tested: the rotor as a free body and the rotor fixed onto the complete setup as used in wind tunnel tests (here referred to as the clamped configuration). All the identified modes for the clamped configuration which can have an effect in the operational domain of the rotors are represented in Fig. 6. They can be divided into two distinct categories: modes of the rotor as a whole (symmetric modes) and modes specific to one of the blades (asymmetric modes). This latter category indicates manufacturing differences between the produced rotor halves. Asymmetric modes tend to come in pairs: both components of such a pair are identical modes but at slightly different frequencies. This is, for example, the case for modes 5 and 6 and modes 8 and 9.

The comparison of the two mentioned configurations allows to identify possible shifts or suppressions of specific modal frequencies. The modal assurance criterion (MAC, (Allemang, 2003),) indicates the similarity between the free configuration and the clamped configuration (Fig. 7). It allows to identify the influence of the experimental setup on the modal frequencies of the rotor. The correlation between the eigenmodes of the two configurations indicates that most modes are shifted to lower frequencies when clamped. This is, however, not the case for the simultaneous up-down mode (mode 1) of the clamped configuration. This mode correlates for over 60% with two free-rotor modes, a lower one 16.2 Hz and a higher one, 39.9 Hz. It is also remarkable that the 77.0 Hz free rotor modal frequency seems to shift to 122.6 Hz. This free-rotor modal frequency corresponds to the oscillating of the blades in a span wise direction. The addition of the main shaft thus makes the rotor more rigid for this kind of excitation. The modes which exhibit the highest correlation are compared numerically in Table 2. The critical damping ratios ( $\zeta$ ) are all evaluated to be reliable as no specific outliers are observed. This modal analysis allows to conclude that the experimental setup does not have a dramatic impact on the vibrational modes of the rotor.

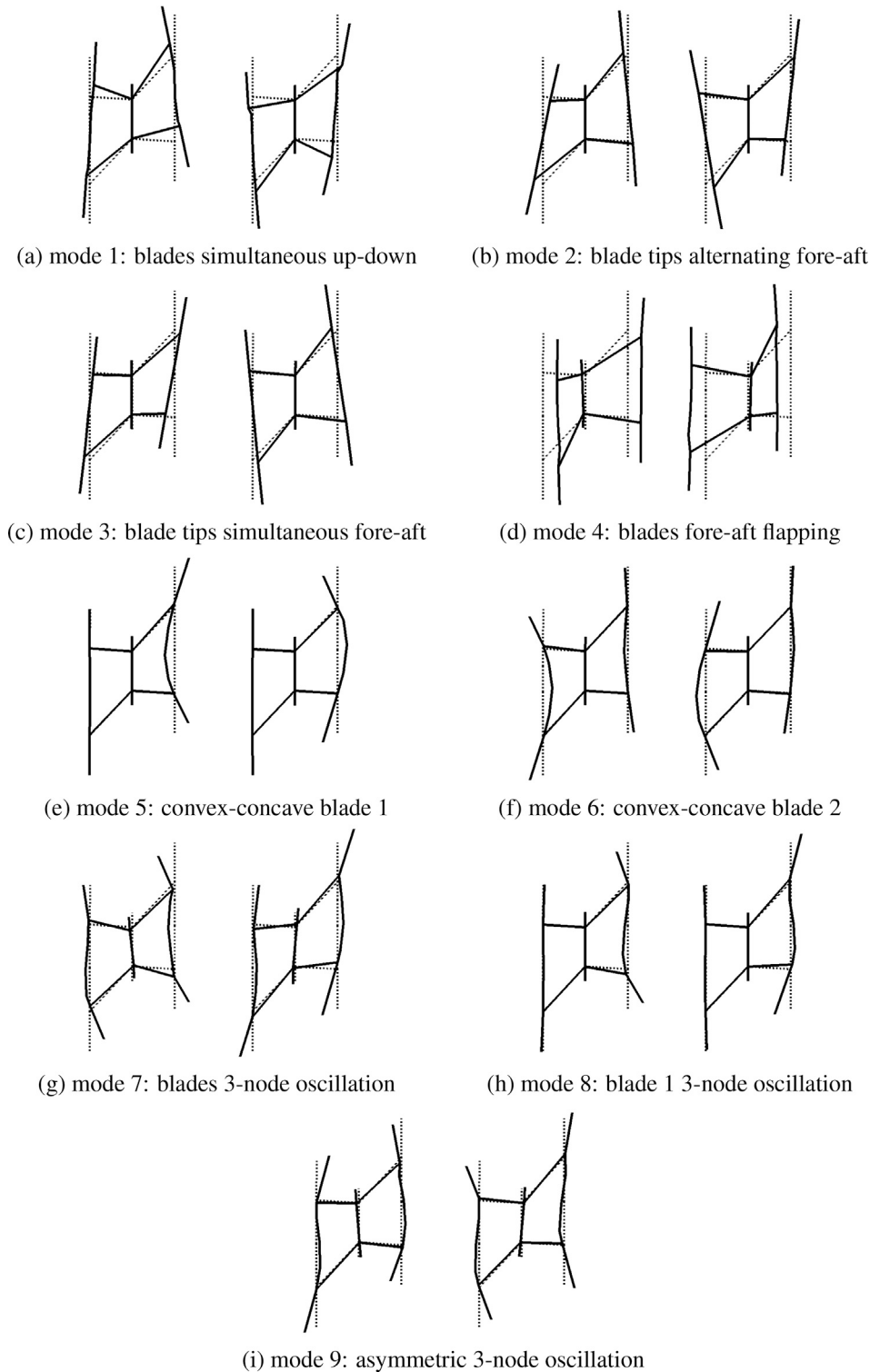


**Fig. 6.** Experimentally observed modal natural frequencies of the rotor over the operating range.

## 5. Characterisation of the turbine setup

### 5.1. Experimental test setup

During wind tunnel tests, the rotors are mounted on top of an aluminium frame which holds the sensors. This frame is also equipped with a generator which is used as a motor during start-up as this VAWT-model is not self-starting. The generator retrieves its main function once

the aerodynamic forces drive the rotor, around tip-speed ratio of 2.4.<sup>1</sup>

To measure the produced mechanical torque and rotational speed, the setup is equipped with a direct drive torque sensor (Lorenz-Messtechnik, DR-3000). This torque sensor is fitted inline between the rotor shaft and

<sup>1</sup> All data further presented and discussed in this manuscript are accessible online: <http://tinyurl.com/VAWTsupportData> or can be requested at the corresponding author.

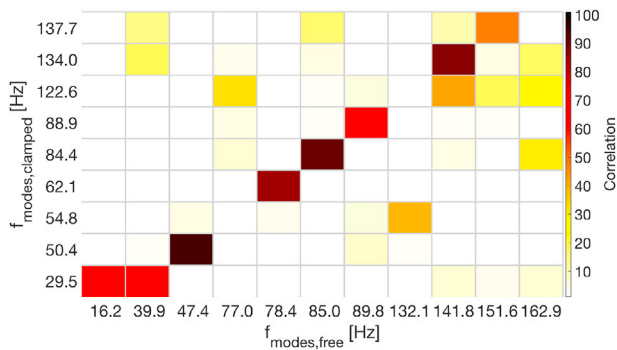


**Fig. 7.** Correlation of the modal frequencies of the rotor as a free body and mounted on the experimental setup as used during wind tunnel tests.

**Table 2**

Modal frequencies of the rotor for clamped and free configurations.

Mode	Clamped		Free	
	f [Hz]	$\zeta$ [%]	f [Hz]	$\zeta$ [%]
1	29.5	0.06	16.2	3.38
			39.9	1.36
2	50.4	0.75	47.4	0.87
3	54.8	0.72	132.1	0.67
4	62.1	0.64	78.4	0.69
5	84.4	1.08	85.0	0.71
6	88.9	0.69	89.8	0.80
7	122.6	0.61	77.0	0.93
8	134.0	0.90	141.8	0.77
9	137.7	0.66	151.6	0.97

the generator shaft. The generator shaft is connected to the motor/generator via a drive belt with gear ratio  $\frac{100}{28}$ . On the rotor shaft side, a one-pulse-per-revolution signal is acquired. This signal indicates the passing of the zero azimuthal position. Finally, a variable resistance circuit is connected to the generator to monitor the generated electrical power and to allow control of the rotational speed.

### 5.2. Drive train losses

A losses test was carried out in order to make a distinction between aerodynamically generated torque and mechanical torque losses in the drive train. To analyse this, the generator was used as a motor to impose a rotation on the drive train without rotor. Once a steady state is reached, the generator shaft is being driven at a constant rotational speed, which on its turn drives the rotor shaft with the torque sensor in-between. In this state, the torque sensor only measures frictional losses in the bearings of the rotor shaft because of the nature of the torque sensor, which measures a differential torque between its input and output side. The motor was used to set various rotational speeds (referred to as plateaus) upon the drive train ranging between 0 and 1120 rpm (1120 rpm corresponds to the maximum possible rotational speed while driving the drive train with the motor). Every plateau was held for approximately 60 s while the back torque was measured. Each measured plateau average and standard deviation is represented in Fig. 8 with the blue error bars. The losses test indicated a maximum torque loss of 3.1 cNm at 1120 rpm (Fig. 8). In terms of power this corresponds to 3.6 W. In order to approximate the losses over the full operating range (indicated by the two vertical lines on Fig. 8) the data was extrapolated with a third-order polynomial to extend over the complete operating range (orange curve in Fig. 8). For the range of operational rotational speeds these losses vary between 8% for the lower part of the operating range and 12% for the higher part of operating range. The power generation is further discussed in Section 5.3.

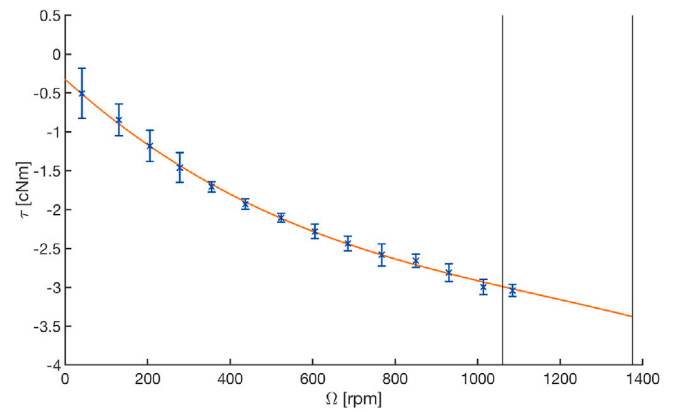


**Fig. 8.** Back torque generated by frictional losses in the bearings fitted with a third-order polynomial and extrapolated to estimate the back torque over the full scope of the operating range (indicated with two vertical lines).

### 5.3. Rotor performance

The torque,  $\tau$ , and rotational speed,  $\Omega$ , are directly recorded by the torque sensor. Taking into account  $U_0$ , the power coefficient,  $C_p$ , is then calculated with the following relationship:

$$C_p = \frac{P_{\text{mech}}}{P_{\text{wind}}} = \frac{\tau \Omega}{\frac{1}{2} \rho D H U_0^3} \quad (10)$$

with the air density denoted by  $\rho$ .

#### 5.3.1. Testing conditions

Both Gen1 rotors were tested in the L1-A wind tunnel of the von Karman Institute at 11.0 m/s and turbulence intensity of 0.3%. The L1-A is a circular open-jet with a diameter of 3 m. On the other hand, the two Gen2 rotors were tested in the Boundary Layer Test Section of the GVPM closed-circuit wind tunnel of the Politecnico di Milano (width = 13.8 m, height = 3.8 m). The Gen2 tests were carried out at a velocity of 10.7 m/s and turbulence intensity of 2%.

#### 5.4. Testing procedure and error propagation

A typical 30-min long measurement of the torque generated by a Gen2 rotor is illustrated in Fig. 9. During such a  $C_p(\lambda)$ -sweep, several steady-state conditions are held to obtain plateaus. Plateaus of which the standard deviation of the rotational speed is greater than  $\sqrt{10}$  rpm are later rejected during post-processing. For this measurement, the

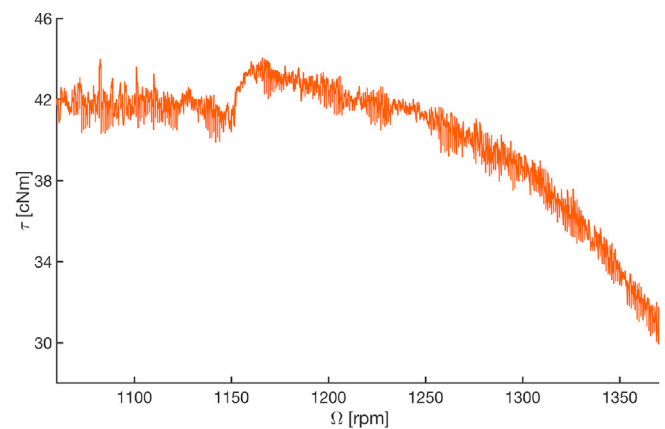


**Fig. 9.** Example of a torque measurement within the operating range. The torque exhibits a discontinuity around 1150 rpm (discussed in Section 5.6). The data has been smoothed over 1 s and corrected for drive train losses.

rotational speed was steadily increased and the data was smoothened over 1 s to reduce the noise on the measured signal. A correction for friction losses in the drive train was also applied. An unstable region, visualised by the discontinuity in Fig. 9, is observed around 1150 rpm. This is further discussed in Section 5.6. Because of manufacturing differences, the second Gen2 rotor does not suffer from this discontinuity in its operational region (the discontinuity is located below the operating region).

The resulting  $C_p(\lambda)$ -curve for the two Gen1 rotors and the two Gen2 rotors exhibit an optimal  $C_p$  between 0.13 and 0.23 (Fig. 10). The standard deviation on the power coefficient and tip-speed ratio are derived via standard error propagation techniques based on the standard deviation of the torque, rotational speed, wind speed and density over an identified plateau (inserted as error bars in the figures). Systematic errors include drive-train losses (corrected), blockage effects (2%, considered negligible) and velocity fluctuations (taken into account in error of  $C_p$ ).

#### 5.4.1. Performance difference

**5.4.1.1. Gen1 rotor 1 vs Gen2 rotor 2.** The relatively large performance difference between the Gen1 rotors (dashed lines on the figure) is caused by the damaging of the moulds in the demoulding process (Section 3.1) and a low torsional resistance of the geometry. Furthermore, one blade of the poorly performing Gen1 rotor contains a misaligned leading edge dramatically impacting its performance. The performance difference between both Gen2 rotors is negligible except for a small difference at tip-speed ratios between 2.6 and 2.8. The difference persists for tip-speed ratios below the observed discontinuity (see Section 5.6).

**5.4.1.2. Gen1 vs Gen2.** The better performing Gen1 rotor exhibits a  $C_p(\lambda)$ -curve which lies on average 10% above the performance of the Gen2 rotors. The results of a Reynolds number sensitivity analysis on the Gen1 rotors are illustrated in Fig. 11. For this analysis, wind tunnel tests were carried out at 7.7 m/s and 11 m/s. At 7.7 m/s, the performance of the Gen1 turbines degrades down to approximately 65% of the performance at 11 m/s indicating a Reynolds number dependency. Part of the difference in performance between the Gen1 and Gen2 rotors can thus be attributed to the different Reynolds number at which the tests were carried out (11.0 m/s vs 10.7 m/s). By considering a linear scaling of  $C_p$  with respect to  $Re_c$ , we can expect a difference in  $C_p$  of 3.4% solely from the velocity difference.

Another difference between the Gen1 and Gen2 testing is the turbulence intensity, which is 0.3% in the L1-A and 2% in the GVPM. The effect of turbulence intensity on the rotors is discussed in (Molina et al., 2018).

Finally, a major design difference between the Gen1 and Gen2 rotors is their shaft (Rezaeiha et al., 2017). concluded that the shaft of the rotors

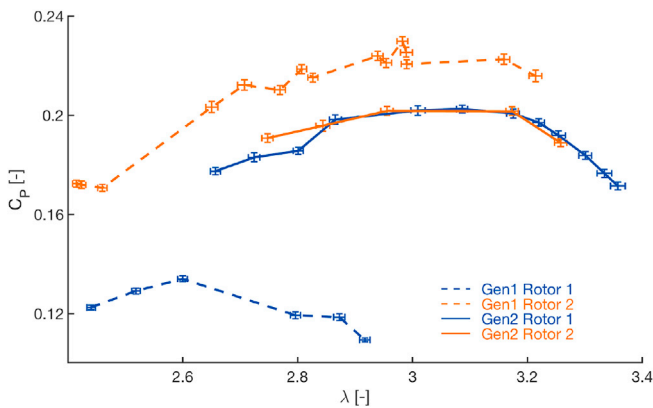


**Figure 10.**  $C_p(\lambda)$  of two Gen1 rotors (orange and blue dashed lines) compared with two Gen2 rotors (orange and blue solid lines). The data has been corrected for drive train losses.

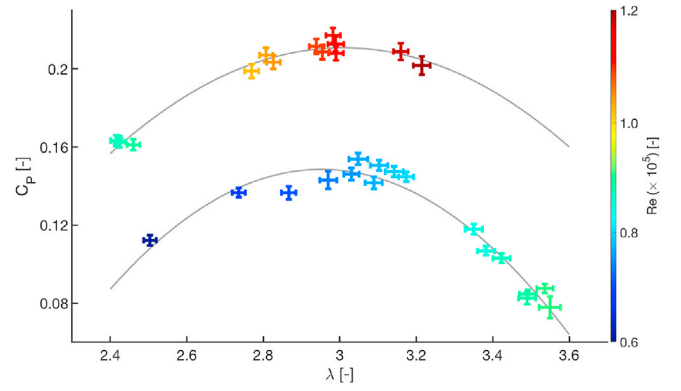


**Fig. 11.** Influence of the Reynolds number on the power coefficient. The error bars indicate twice the standard deviation for clarity. The fitted curves serve no other purpose than to distinguish the two different tests.

is expected to degrade the performance of the VAWT based on their shaft-to-turbine diameter ratio. With a shaft-to-turbine diameter ratio of 0.06, the aerodynamic performance of the Gen1 rotors is expected to induce a 3.1%  $C_p$ -loss while the larger shaft-to-turbine diameter ratio of the Gen2 rotors (0.10) will entail a 1.4% larger degradation of  $C_p$ .

Of the approximately 10% difference between the  $C_p$  of Gen1 and Gen2, 5% can be accounted for by the different Reynolds number and shaft size. Furthermore, it was studied that the turbulence intensity will also contribute to differences in performance. The different SR is likely to have an impact as well on the  $C_p$ .

#### 5.5. Interpretation of dynamic torque

To interpret dynamic measurements, the drive train is approximated as a one degree-of-freedom system: two infinitely stiff mass moments of inertia (denoted by  $J$ ) connected by a torque sensor (massless torsional spring with  $k_t = 3.7 \times 10^2$  Nm/rad).

For simplicity of notation, the rotor side is denoted by the index 1 and the generator side by the index 2. According to Newton's second law, the equation of motion (neglecting damping) is given by:

$$J_1 J_2 (\ddot{\theta}_1 - \ddot{\theta}_2) + k_t (J_1 + J_2) (\theta_1 - \theta_2) = J_2 \tau_1 - J_1 \tau_2. \quad (11)$$

In general, the frequency of the dynamic torque should be well below the natural frequency of the measurement system (the drive train). A margin of 30% is recommended in the manual of the torque sensor. Given that the experimentally determined values for  $J_1$  and  $J_2$  are 0.0263 kg, m<sup>2</sup> and 0.0012 kg, m<sup>2</sup> respectively, the first natural torsional frequency,  $\omega_n$ , of the system is 89 Hz. This  $\omega_n$  implies that dynamic torques with frequencies up to about 60 Hz can be measured. This will prove to be insufficient, given that the dynamic torque can be expected to contain multiple harmonic components of the fundamental angular frequency (which ranges from 15 Hz to 25 Hz). Therefore, components with frequencies above 60 Hz will be distorted by the measurement system itself.

Equation (11) also indicates that the measured torque  $k_t(\theta_1 - \theta_2)$  does not correspond directly to the aerodynamic torque  $\tau_1$ . The torque sensor measurement is a function of the weighted difference between the aerodynamic driving torque and the generator back torque. The larger  $J_1$  is with respect to the sum  $J_1 + J_2$ , the more the measured torque will be influenced by  $\tau_2$ , and thus the more it will diverge from the aerodynamic torque.

Equation (11) nicely illustrates the difficult balance that the design of a test setup entails:

- If a rotary torque transducer is employed, as in our setup, the sensitivity scales inversely with  $k_t$ , and thus inversely with the bandwidth for the dynamic torque measurements.



- A high value of  $J_2$  with respect to the total  $J_1 + J_2$  is required to maximally suppress distortions from  $\tau_2$ , but increasing  $J_2$  reduces the natural frequency and thus the bandwidth.
- If, as for our setup,  $k_t$  is limited by the maximum expected torque (which is mainly kept low by the small size of the model), and  $J_1$  is low (limited by the high rotational speed required to achieve the right range in tip-speed ratios and Reynolds numbers), then we can only accept that the measured dynamic torque variations will be too large extent influenced by small distortions coming from  $\tau_2$ . The average measured torque (say, over multiple full rotations at fixed rpm), however, corresponds to the aerodynamic torque (which is equal to the opposite of  $\tau_2$ ) and does not need to be corrected.

If unsteady aerodynamic torque measurements are required, one should resort to the use of strain gauges, either on the struts or the shaft, at an increased cost and complexity to perform the measurements. The much higher stiffness can allow for a much higher  $J_2$  to be used, and eq. (11) can be used for the correction.

The gained insights with regards to dynamic measurements are well appreciated through the analysis of the spectral content of the measured torque, discussed in the following section.

### 5.6. Spectral analysis of the torque measurements

The spectral content of the torque signal was analysed through a spectrogram. This spectrogram (Fig. 12) is based on the same time series as shown in Fig. 9. In this spectrogram, energetic peaks are observed which even persevere in the higher range of the frequency spectrum.

Two spectral components can be distinguished from one another. A first component (and its harmonics) corresponds to the angular frequency of the rotor ( $nP_R$ ,  $n \in \mathbb{N}_0$ ). These spectral components are highlighted on the figure with solid lines. Noticeably, the even multiples of  $1P_R$  appear more energetic, which is a consequence of the symmetric design of the rotor. This can, for example, be observed by comparing  $1P_R$  and  $2P_R$  or  $5P_R$  and  $6P_R$ .

A second main spectral component is identified as the belt passing frequency (BPF or  $1P_B$ ) which is lower than  $1P_R$ . When a BPF harmonic ( $nP_B$ ,  $n \in \mathbb{N}_0$ ) lies adjacent to a harmonic of the angular frequency, they co-excite torque ripples. This is the case for  $4P_R$  and  $7P_B$  which co-excite

the region between 70 Hz and 91 Hz.

Torque ripples around the first torsional natural frequency (the time-invariant yellow band around 89 Hz on Fig. 12) are magnified due to the natural torsional frequency of the system. Because of this natural frequency, the  $4P_R$  and  $7P_B$  harmonics dominate the spectrum; they are even more energetic than the fundamental frequency of the aerodynamic torque variations,  $2P_R$ .

### 5.7. Operational modal analysis

To assess the excitation of the different modes during operation of the rotor, the rotational speed (1P) and its harmonic components ( $nP$ , where  $n \in \mathbb{N}_0$ ) are compared to the modal frequencies of the rotor (Fig. 13). On this Campbell diagram, the crosses indicate which modes (horizontal lines on the figure) will be excited over the operational regime by the rotational speed or multiples of this one. No crossings of the 1P and 2P components with modal frequencies occur over this operational regime, which is indicated with the highlighted zone. All the other harmonic components, however, do cross various modes which will be excited. The symmetry of the rotor design makes that even harmonics of the rotational

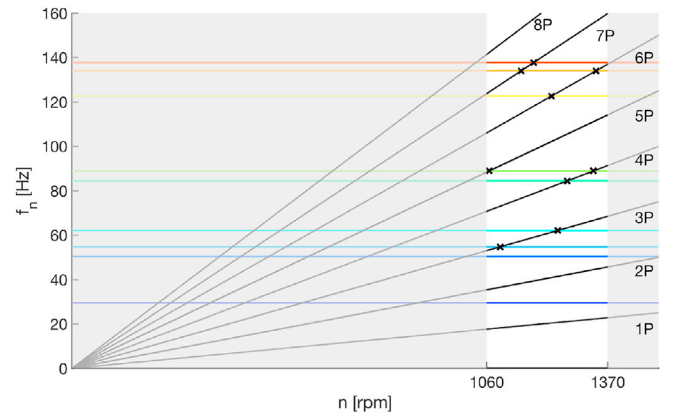


Fig. 13. Campbell diagram of the modal frequencies of the rotor compared to the operational rotational frequencies.

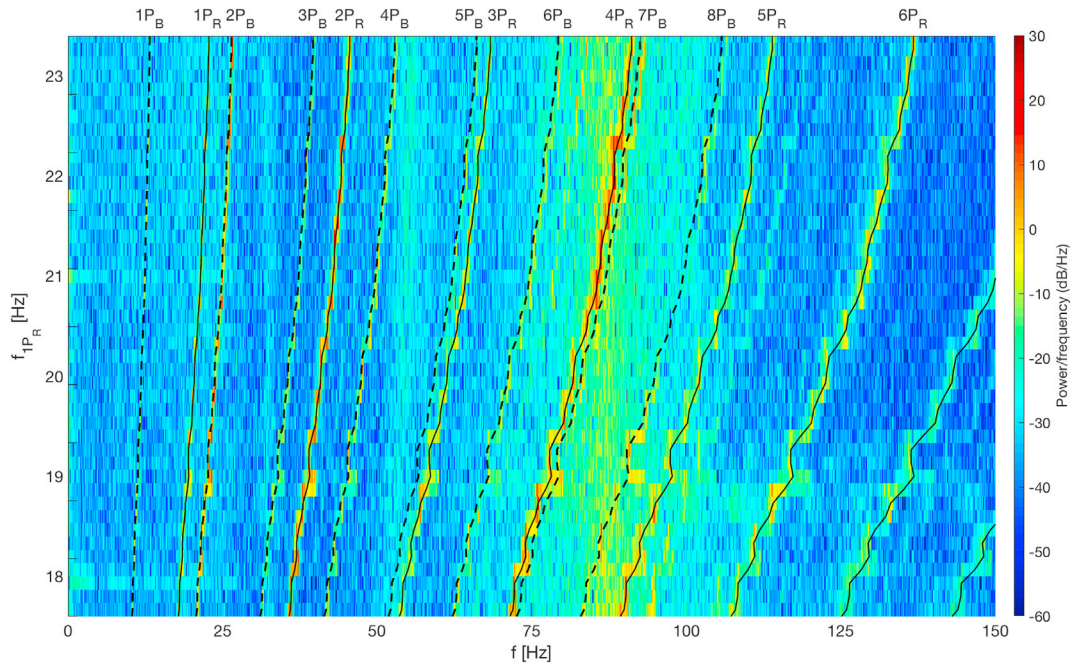


Fig. 12. Spectral content of a torque measurement for a tip-speed ratio sweep.

speed are likely to be more energetic than uneven ones.

Two pairs of modal frequencies can be distinguished on Fig. 13: a first pair around 85 Hz and a second pair around 135 Hz. These are asymmetric modes as (Section 4.4), where the small difference in frequency between modes 5 and 6 and between modes 8 and 9 is due to manufacturing imperfections. Because such modes create an unbalance of the forces, thereby influencing the torque generation.

Table 3 summarises the modes which are excited by the rotational speeds or harmonic components of this one. Remarkably, mode 8 gets excited by the 7th harmonic of the rotational speed at 1149 rpm which corresponds to the discontinuity observed in Fig. 9.

### 5.8. Rotor near wake velocity profiles

The unification of the two-part rotor hub (difference between Gen1 and Gen2) improved the torsional stiffness of the rotor but is expected to decrease the performance. A wider and longer shaft will influence the characteristics of the turbine wake. This turbine wake is a recurrent field of study on VAWT research ((Tescione et al., 2014; Bianchini et al., 2017; Hohman et al., 2018)). A series of measurements were performed in the near wake of the rotor (0.75D downstream of the rotating shaft). Two horizontal velocity profiles were measured, one at height 0.5H (midplane of the rotor) and one at 0.86H (to avoid the influence of the shaft or tip effects in the wake) (see Fig. 14a).

**Table 3**  
Modal excitations through rotational speed and its harmonics.

Harmonic	Excitation 1	$n_1$ [rpm]	Excitation 2	$n_2$ [rpm]
1P	-	-	-	-
2P	-	-	-	-
3P	mode 3	1095	mode 4	1242
4P	mode 5	1267	mode 6	1333
5P	mode 6	1067	-	-
6P	mode 7	1226	mode 8	1340
7P	mode 8	1149	mode 9	1180
8P	-	-	-	-

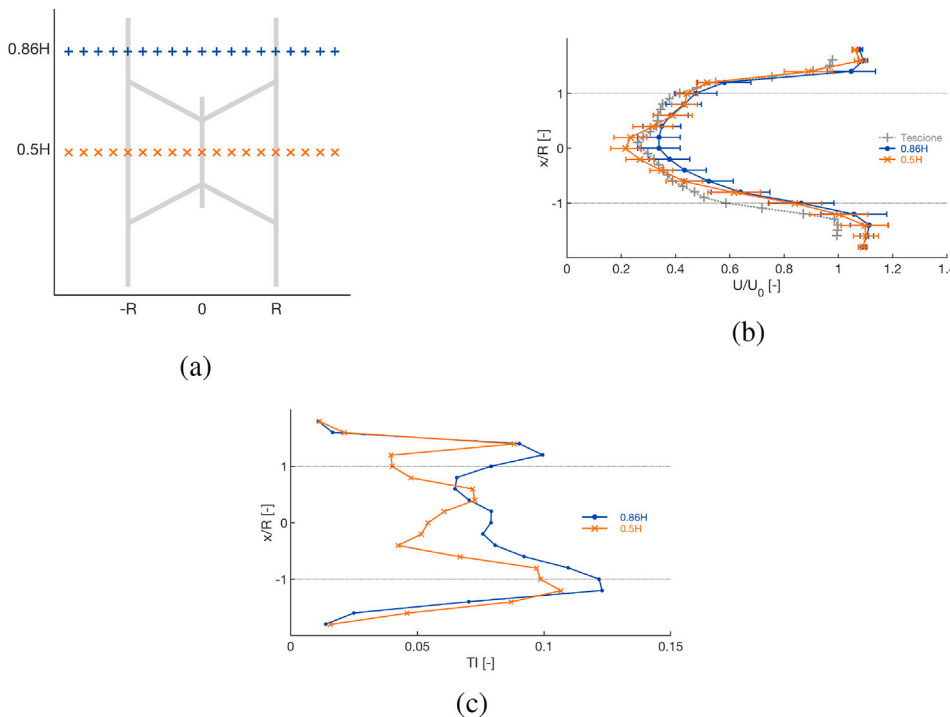


**Fig. 14.** (a) Positions of the two measured velocity profiles 0.75D behind the rotor. (b) Normalised velocity profiles 0.75D behind the rotor (solid lines with orange crosses, blue dots) compared with the data of (Tescione et al., 2014) (dotted line with grey crosses). The error bars correspond to one standard deviation of the velocity. (c) Local turbulence intensity 0.75D behind the rotor. (For interpretation of the references to colour in this figure legend, the reader is referred to the Web version of this article.)

The results are presented in terms of normalised velocity with the unperturbed velocity (9 m/s) (Fig. 14b). The error bars correspond to the standard deviation of the velocity during a measurement. The rotational speed is 1070 rpm (18 Hz) which results in a tip-speed ratio of 3 and a mean-chord based Reynolds number of  $1 \times 10^5$ . For both velocity profiles, the normalised velocity is larger at the side of the downwind moving blade (negative half of the velocity profiles) compared to the upwind moving blade (positive half of the velocity profiles). The two profiles differ, however, with regard to their extreme values. Behind the rotor shaft the wind velocity is reduced to 22% of its unperturbed condition. Without the influence of the shaft the reduction is limited to 34% of the unperturbed condition. That value presents a good agreement with previous experiments on a 2-bladed VAWT from (Tescione et al., 2014), which suggests that the increase of the shaft diameter indeed has a significant effect in the near wake. The shape and characteristics of the rotor wake are nonetheless consistent with previous findings, which validates the possibility to use this model for VAWT wake studies.

When the standard deviations (the error bars from Fig. 14b) are divided by the freestream wind speed, one obtains a measure of the level of local turbulence intensity, TI, in the near wake (Fig. 14c). Apart from a shift towards positive  $x/R$  (visible in Fig. 14b and c) due to the deflection of the wake, Fig. 14c clearly shows distinct regions of increased TI in the wake. The increase near  $x/R = 0.5$  at 0.5H is likely to be caused by the shaft wake as is further underlined by the absence of this increase at 0.86H. The increased levels of TI at  $x/R = +/ - 1$ , on the other hand, can be related to blade aerodynamics: a spectral analysis of the velocities revealed that the standard deviation originates from harmonic variations at 1P and 2P frequencies. Although vorticity could not be measured in our setup, the presence of harmonic components in the wake are quite suggestive of the occurrence of dynamic stall. A more complete study and comparison with CFD simulations is presented in (Molina et al., 2018).

## 6. Conclusion and future work

This article presents the different steps (design, manufacturing and validation) required to prepare an H-type Darrieus rotor setup for wind

tunnel tests. The design requirements of the rotor are summarised, and the impact on design choices and manufacturing is discussed. The quality of the carbon-fibre rotor blades is assessed and proven to be repeatable. This is important, as the small scale of the rotors makes the aerodynamic performance sensitive to geometric imperfections.

Structural, mechanical and aerodynamic aspects are carefully analysed through various tests. Structural tests confirmed that the designed and manufactured VAWT rotors ensure safe wind tunnel tests, i.e. during operation the rotor models rotate at 60% of their critical rotational speed.

A spectral analysis of the generated torque by the rotor during operation indicated that higher harmonics distort the torque measurements. Above that, a first natural torsional frequency and torque ripples on the generator side contribute to this distortion. These two contaminations were predicted numerically. Comparing the harmonics, which are retrieved in the spectral content of the torque measurement, with the results of an experimental modal analysis allowed to identify modes which impact the torque production. This modal analysis revealed two kinds of modal vibrations: symmetric ones and asymmetric ones. The asymmetric modes appeared to influence the performance of the rotor. The operational modal analysis confirmed this: when specific modes are excited by a harmonic component of the rotational speed, they tend to disrupt the normal operation of the rotor.

Because the torque sensor measures the aerodynamic torque contaminated with other components, it requires a complete understanding of the experimental setup to measure unsteady aerodynamics. Structural dynamics of the rotor, drive train and sensor must be characterised to be able to interpret unsteady aerodynamics experimentally. Future work will entail the development of a correction for aerodynamic torque measurements to achieve a reliable interpretation of the unsteady torque measurements.

## Acknowledgements

The financial support of Nenuphar is gratefully acknowledged.

## References

- Akins, R.E., Berg, D.E., Cyrus, W.T., 1987. Measurements and Calculations of Aerodynamic Torques for a Vertical-axis Wind Turbine, Tech. Rep. SAND86-2164. Sandia National Laboratories.
- Allemang, R., 2003. The modal assurance criterion - twenty years of use and abuse. *Sound Vib.* 37, 14–23.
- Asr, M.T., Masoumi, M.M., Mustapha, F., 2017. Modal behaviour of vertical axis wind turbine comprising prestressed rotor blades: a finite element analysis. *Pertanika J. Sci. Technol.* 25, 977–982. ISSN 0128-7680; EISSN: 2231-8526.
- Bachant, P., Wosnik, M., 2016. Effects of Reynolds number on the energy conversion and near-wake dynamics of a high solidity vertical-axis cross-flow turbine. *Energies* 9 (2), 73. ISSN 1996-1073, wOS:000371831900004.
- Balduzzi, F., Bianchini, A., Carnevale, E.A., Ferrari, L., Magnani, S., 2012. Feasibility analysis of a Darrieus vertical-axis wind turbine installation in the rooftop of a building. *Appl. Energy* 97, 921–929. ISSN 0306-2619.
- Bayati, I., Foletti, S., Tarsitano, D., Belloli, M., 2018. A reference open data vertical axis wind turbine, with individual pitch control, for code validation purposes. *Renew. Energy* 115 (Suppl. C), 711–720. ISSN 0960-1481.
- Bertényi, T., Wickins, C., McIntosh, S., 2010. Enhanced energy capture through gust-tracking in the urban wind environment. In: 48th AIAA Aerospace Sciences Meeting Including the New Horizons Forum and Aerospace Exposition. American Institute of Aeronautics and Astronautics, pp. 1376–1382.
- Bianchini, A., Balduzzi, F., Bachant, P., Ferrara, G., Ferrari, L., 2017. Effectiveness of two-dimensional CFD simulations for Darrieus VAWTs: a combined numerical and experimental assessment. *Energy Convers. Manag.* 136 (Suppl. C), 318–328. ISSN 0196-8904.
- Borg, M., Shires, A., Collu, M., 2014. Offshore floating vertical axis wind turbines, dynamics modelling state of the art. part I: Aerodynamics. *Renew. Sustain. Energy Rev.* 39 (Suppl. C), 1214–1225. ISSN 1364-0321.
- Bottasso, C.L., Campagnolo, F., Petrović, V., 2014. Wind tunnel testing of scaled wind turbine models: beyond aerodynamics. *J. Wind Eng. Ind. Aerodyn.* 127 (11–28). ISSN 0167-6105.
- Brusca, S., Lanzafame, R., Messina, M., 2014. Design of a vertical-axis wind turbine: how the aspect ratio affects the turbine's performance. *Int. J. Energy Environ. Eng.* 5 (4), 333–340. ISSN 2008-9163, 2251-6832.
- Chatelain, P., Duponcheel, M., Caprace, D.-G., Marichal, Y., Winckelmans, G., 2007. Vortex Particle-Mesh simulations of Vertical Axis Wind Turbine flows: from the blade aerodynamics to the very far wake. *J. Phys. Conf. Ser.* 753.
- Cheng, Z., Madsen, H.A., Gao, Z., Moan, T., 2017. Effect of the Number of Blades on the Dynamics of Floating Straight-Bladed Vertical axis Wind Turbines. *Renew. Energy* 101, 1285–1298. ISSN 0960-1481.
- Clark, R., 1991. Design and initial performance of a 500-kw vertical-Axis wind turbine. *Trans. ASAE* 34 (3), 985–991. ISSN 0001-2351, wOS:A1991GD09800041.
- Dabiri, J.O., 2011. Order-of-magnitude enhancement of wind farm power density via counter-rotating vertical-axis wind turbine arrays. *J. Renew. Sustain. Energy* 3, 043104.
- Delafin, P.L., Nishino, T., Wang, L., Kolios, A., 2016. Effect of the number of blades and solidity on the performance of a vertical axis wind turbine. *J. Phys. Conf. Ser.* 753, 022033. ISSN 1742-6596.
- Dossena, V., Persico, G., Paradiso, B., Battisti, L., Dell'Anna, S., Brighenti, A., Benini, E., 2015. An experimental study of the aerodynamics and performance of a vertical axis wind turbine in a confined and unconfined environment. *J. Energy Resour. Technol.* 137 (5), 051207. ISSN 0195-0738.
- Duraissamy, K., Lakshminarayan, V., 2014. Flow physics and performance of vertical Axis wind turbine arrays. In: 32nd AIAA Applied Aerodynamics Conference.
- Elkhoury, M., Kiwata, T., Aoun, E., 2015. Experimental and numerical investigation of a three-dimensional vertical-axis wind turbine with variable-pitch. *J. Wind Eng. Ind. Aerodyn.* 139, 111–123. ISSN 0167-6105.
- Greenblatt, D., Schulman, M., Ben-Harav, A., 2012. Vertical axis wind turbine performance enhancement using plasma actuators. *Renew. Energy* 37, 345–354.
- Hohman, T.C., Martinelli, L., Smits, A.J., 2018. The effects of inflow conditions on vertical axis wind turbine wake structure and performance. *J. Wind Eng. Ind. Aerodyn.* 183 (1–18). ISSN 0167-6105.
- Huijs, F., Vlasveld, E., Gormand, M., Savenije, F., Caboni, M., LeBlanc, B., Simao Ferreira, C., Lindenburg, K., Gueydon, S., Otto, W., Paillard, B., 2018. Integrated design of a semi-submersible floating vertical axis wind turbine (VAWT) with active blade pitch control. *J. Phys. Conf. Ser.* 1104, 012022.
- LeBlanc, B.P., Simao Ferreira, C.J., 2018. Experimental determination of thrust loading of a 2-bladed vertical Axis wind turbine. *J. Phys. Conf. Ser.* 1037, 022043.
- Li, Q., Maeda, T., Kamada, Y., Murata, J., Furukawa, K., Yamamoto, M., 2015. Effect of number of blades on aerodynamic forces on a straight-bladed Vertical Axis Wind Turbine. *Energy* 90, 784–795. ISSN 0360-5442.
- Li, Q., Maeda, T., Kamada, Y., Murata, J., Furukawa, K., Yamamoto, M., 2016. The influence of flow field and aerodynamic forces on a straight-bladed vertical axis wind turbine. *Energy* 111, 260–271. ISSN 0360-5442.
- Mabrouk, I.B., El Hami, A., Walha, L., Zghal, B., Haddar, M., 2017. Dynamic vibrations in wind energy systems: application to vertical axis wind turbine. *Mech. Syst. Signal Process.* 85, 396–414. ISSN 0888-3270.
- McLaren, K., Tullis, S., Ziada, S., 2012. Measurement of high solidity vertical axis wind turbine aerodynamic loads under high vibration response conditions. *J. Fluids Struct.* 32 (12–26). ISSN 0889-9746.
- Miller, M.A., Duvvuri, S., Brownstein, I., Lee, M., Dabiri, J.O., Hultmark, M., 2018. Vertical-axis wind turbine experiments at full dynamic similarity. *J. Fluid Mech.* 844, 707–720. ISSN 0022-1120, 1469-7645.
- Molina, A.C., Massai, T., Balduzzi, F., Bianchini, A., Ferrara, G., De Troyer, T., Bartoli, G., 2018. Combined experimental and numerical study on the near wake of a Darrieus VAWT under turbulent flows. *J. Phys. Conf. Ser.* 1037 (7), 072052. ISSN 1742-6596.
- Möllerström, E., Ottermo, F., Goude, A., Eriksson, S., Hylander, J., Bernhoff, H., 2016. Turbulence influence on wind energy extraction for a medium size vertical axis wind turbine. *Wind Energy* 19 (11), 1963–1973. ISSN 1099-1824.
- Paraschivoiu, I., 1981. Double-multiple streamtube model for Darrieus wind turbines. In: *Wind Turbine Dynamics*, 1, pp. 19–25.
- Paraschivoiu, I., 2002. *Wind Turbine Design: with Emphasis on Darrieus Concept*. Polytechnic International Press, Quebec, Canada. ISBN 978-2-553-57500931-0, google-Books-ID: seVtnVgso0C.
- Parneix, N., Fuchs, R., Immas, A., Silvert, F., Deglaire, P., 2016. Efficiency improvement of vertical-axis wind turbines with counter-rotating lay-out. *Wind Eur. (EAWF) Proc.* 8.
- Paulsen, U.S., Madsen, H.A., Hattel, J.H., Baran, I., Nielsen, P.H., 2013. Design optimization of a 5 MW floating offshore vertical-axis wind turbine. *Energy Procedia* 35 (Suppl. C), 22–32. ISSN 1876-6102.
- Peng, Y.-X., Xu, Y.-L., Zhan, S., Shum, K.-M., 2019. High-solidity straight-bladed vertical axis wind turbine: aerodynamic force measurements. *J. Wind Eng. Ind. Aerodyn.* 184, 34–48. ISSN 0167-6105.
- Rezaeiha, A., Kalkman, I., Montazeri, H., Blocken, B., 2017. Effect of the shaft on the aerodynamic performance of urban vertical axis wind turbines. *Energy Convers. Manag.* 149, 616–630. ISSN 0196-8904.
- Rezaeiha, A., Montazeri, H., Blocken, B., 2018. Towards optimal aerodynamic design of vertical axis wind turbines: impact of solidity and number of blades. *Energy* 165, 1129–1148. ISSN 0360-5442.
- Sheldahl, R.E., Klimas, P.C., 1981. Aerodynamic Characteristics of Seven Symmetrical Airfoil Sections through 180-degree Angle of Attack for Use in Aerodynamic Analysis of Vertical axis Wind Turbines, Tech. Rep. SAND-80-2114. Sandia National Labs., Albuquerque, NM (USA).
- Sheldahl, R.E., Klimas, P.C., Feltz, L.V., 1980. Aerodynamic Performance of a 5-Metre-Diameter Darrieus Turbine with Extruded Aluminum NACA-0015 Blades, 80–0179. Sandia National Laboratories.
- Shires, A., 2013. Design optimisation of an offshore vertical axis wind turbine. *Proc. ICE Energy* 166 (7–18). ISSN 1751-4223.
- Simão Ferreira, C., Geurts, B., 2015. Aerofoil Optimization for Vertical-axis Wind Turbines. *Wind Energy*.
- Simão Ferreira, C., Madsen, H.A., Barone, M., Roscher, B., Deglaire, P., Arduin, I., 2014. Comparison of aerodynamic models for vertical Axis wind turbines. *J. Phys. Conf. Ser.* 524 (1), 012125.

- Sutherland, H.J., Berg, D.E., Ashwill, T.D., 2012. A Retrospective of VAWT Technology, Tech. Rep. SAND2012-0304. Sandia National Laboratories.
- Tescione, G., Ragni, D., He, C., Simão Ferreira, C.J., van Bussel, G.J.W., 2014. Near wake flow analysis of a vertical axis wind turbine by stereoscopic particle image velocimetry. *Renew. Energy* 70 (61), 47. ISSN 0960-1481.
- Timmer, W., 2008. Two-dimensional low-Reynolds number wind tunnel results for airfoil NACA 0018. *Wind Eng.* 32 (6), 525–537.
- G. van Bussel, S. Mertens, Small Wind Turbines for the Built Environment, EACWE4 - The Fourth European & African Conference on Wind Engineering.
- Vergaerde, A., De Troyer, T., Kluczevska-Bordier, J., Parneix, N., Silvert, F., Runacres, M.C., 2018. Wind tunnel experiments of a pair of interacting vertical-axis wind turbines. *J. Phys. Conf. Ser.* 1037, 072049. JPCS.
- Zanforlin, S., Nishino, T., 2016. Fluid dynamic mechanisms of enhanced power generation by closely spaced vertical axis wind turbines. *Renew. Energy* 99, 1213–1226.